catalysts

MDPI

Article

Accelerated Photodegradation of Organic Pollutants over BiOBr/Protonated g-C_3N_4

Juanjuan Liu [1,*], Heng Guo [1], Haoyong Yin [1], Qiulin Nie [1] and Shihui Zou [2,*]

[1] College of Materials & Environmental Engineering, Hangzhou Dianzi University, Hangzhou 310036, China
[2] Key Lab of Applied Chemistry of Zhejiang Province, Department of Chemistry, Zhejiang University, Hangzhou 310027, China
* Correspondence: liujuanjuan0324@hdu.edu.cn (J.L.); shihuizou@zju.edu.cn (S.Z.)

Abstract: Interfacial engineering has emerged as an effective strategy to optimize the photocatalytic activity of heterojunctions. Herein, the interface between graphitic carbon nitride (g-C_3N_4) and BiOBr was readily regulated by a protonation treatment. The synthesized BiOBr/g-C_3N_4 heterojunctions were characterized by X-ray diffraction, scanning electron microscopy, X-ray photoelectron spectroscopy, and UV-Vis diffuse reflectance spectroscopy. The results show that pretreating g-C_3N_4 in diluted HCl solution led to a partial protonation of g-C_3N_4, which ensured intimate contact and high dispersion of supported BiOBr without changing the surface area, bulk g-C_3N_4 structure, or visible light absorption. The abundant BiOBr/g-C_3N_4 interfaces remarkably improved the separation and transfer of photogenerated carriers, which produced more h^+ and $O_2^{\bullet-}$ to accelerate the photocatalytic degradation of organic pollutants. The photocatalytic activities of the BiOBr/g-C_3N_4 heterojunctions were evaluated by the degradation of RhB under visible-light irradiation ($\lambda \geq 420$ nm). The apparent reaction (pseudo-first-order) rate constant of BiOBr supported on partially protonated g-C_3N_4 (Bpg-C_3N_4-0.75) is ca. 3-fold higher than that of BiOBr supported on pristine g-C_3N_4 (Bg-C_3N_4), verifying interfacial engineering as an effective strategy to optimize the catalytic activity of heterojunctions.

Keywords: protonation; g-C_3N_4; BiOBr; heterojunction; organic pollutants

check for updates

Citation: Liu, J.; Guo, H.; Yin, H.; Nie, Q.; Zou, S. Accelerated Photodegradation of Organic Pollutants over BiOBr/Protonated g-C_3N_4. *Catalysts* **2022**, *12*, 1109. https://doi.org/10.3390/catal12101109

Academic Editors: Victorio Cadierno and Raffaella Mancuso

Received: 30 August 2022
Accepted: 21 September 2022
Published: 25 September 2022

1. Introduction

With organic pollutant-induced water contamination becoming a serious global issue, the development of efficient and green technologies to degrade organic pollutants has become increasingly important. As a kind of advanced oxidation process, semiconductor-based photocatalysis has been frequently used to degrade organics in wastewater. [1] However, the high recombination rates of photogenerated electron–hole pairs in a single photocatalyst limit the reaction efficiency. Heterojunction has emerged as a potential solution to address this problem. [2–6] Successful fabrication of heterojunctions relies on not only the selection of suitable lattice and energy-level-matched semiconductors but also on the engineering of a heterojunction interface. [7–9] For a given heterojunction, the intimate and large-area contact interface facilitates the separation and transfer of photogenerated carriers, [10] which motivates researchers to engineer interfacial heterojunctions. For example, in our previous study [7], we reported that the abundant BiOI/ZnO interfaces resulting from the high dispersion of BiOI on ZnO can promote the separation and transfer of photogenerated carriers. Peng et al. [11] fabricated a face-to-face heterojunction of BiOCl/Bi_2WO_6 by in situ topotactic transformation, which exhibited improved photocatalytic activity for tetracycline degradation under visible light. Yang et al. [12] prepared BiOBr/pg-C_3N_4 by an electrostatically driven in situ growth method and reported the critical role of intimate interfaces in photocatalytic degradation of rhodamine B (RhB).

Graphite carbon nitride (g-C_3N_4) is a novel non-metallic semiconductor and has been frequently used to fabricate heterojunctions. [13–17] The heterointerface in g-C_3N_4-based heterojunctions can be readily regulated by the dispersion of supported semiconductors [18–20].

However, the typical methods for enhancing dispersion are usually associated with the modification of the bulk structure and the surface area of g-C_3N_4, which adds new variables that affect the catalytic efficiency of heterojunctions. To reveal the intrinsic influence of heterointerfaces in g-C_3N_4-based heterojunctions, it is desired yet challenging to develop a method that can achieve high dispersion of supported semiconductors without changing the bulk g-C_3N_4 structure, surface area, and light absorption properties.

Herein, we report a partial protonation of g-C_3N_4 that can achieve high dispersion of supported BiOBr without changing the surface area, bulk g-C_3N_4 structure, and visible light absorption of BiOBr/g-C_3N_4 heterojunctions. g-C_3N_4 were prepared by the calcination of melamine. A subsequential pretreatment in diluted HCl solution (X mL HCl in 10 mL H_2O, X = 0, 0.25, 0.5, 0.75 and 1.0) led to a partial protonation of g-C_3N_4, denoted as pg-C_3N_4-X. Dispersing pg-C_3N_4-X in $Bi(NO_3)_3$ solution, followed by the addition of KBr, produced BiOBr/pg-C_3N_4-X heterojunctions. The intrinsic structure–property relationship of the heterointerface in BiOBr/g-C_3N_4 heterojunctions is discussed herein on the basis of the comparison between BiOBr supported on protonated (Bpg-C_3N_4-X) and pristine g-C_3N_4 (Bg-C_3N_4).

2. Results and Discussion

Figure 1a shows the X-ray diffraction (XRD) patterns of Bg-C_3N_4 and Bpg-C_3N_4-X (X = 0.25, 0.50, 0.75, 1.00) samples. Interestingly, all the samples exhibit similar peaks at 13.1° and 27.4°, corresponding to (001) and (002) planes of g-C_3N_4 (JCPDS card No. 87-1526) [21]. No obvious changes in peak shape and location are observed, suggesting that the protonation treatment exerts little influence on the bulk structure of C_3N_4, likely because the protonation of g-C_3N_4 occurs in diluted HCl solution, which modifies the surface charge but does not change the bulk structure of g-C_3N_4. The similar surface areas (ca. 10 $m^2 \cdot g^{-1}$) of g-C_3N_4, pg-C_3N_4-X, Bg-C_3N_4, and Bpg-C_3N_4-X further exclude the exfoliation of bulk g-C_3N_4. Other peaks located at 10.9°, 25.2°, 31.7°, 32.2°, 46.3°, and 57.2° can be readily indexed to (001), (101), (102), (110), (200), and (212) planes of tetragonal phase BiOBr (JCPDS card No. 85-0862), respectively [8]. However, the shape of these diffraction patterns varies. In particular, the samples exhibit very different diffraction intensity ratios of (110)/(102) planes. In the literature [22,23], the I_{110}/I_{102} ratio has been frequently investigated to illustrate the preferential orientation of BiOBr because (110) and (102) planes correspond to the major peaks of the XRD profile and are the lateral surfaces for BiOBr with [010] orientation. Changes in the I_{110}/I_{102} ratio indicate the differential growth behavior of BiOBr. In the standard card of BiOBr (JCPDS: 85-0862), the I_{110}/I_{102} ratio is lower than 1.0. As shown in Figure 1b, the I_{110}/I_{102} ratio increases from 1.19 for Bg-C_3N_4 and 1.98 for Bpg-C_3N_4-0.50 to 2.35 for Bpg-C_3N_4-0.75 and then decreases to 1.94 for Bpg-C_3N_4-1.0. The significantly higher I_{110}/I_{102} ratio relative to the standard ratio (<1.0) indicates that BiOBr preferably grows along (110) orientations on pg-C_3N_4. The variation in the I_{110}/I_{102} ratio with the X in Bpg-C_3N_4-X, on the other hand, suggests that the preferential orientation of BiOBr is influenced by the protonation treatment of g-C_3N_4 support. [24] The highest I_{110}/I_{102} ratio is achieved by Bpg-C_3N_4-0.75, indicating that median protonation is beneficial. Considering that all the samples have similar surface area and bulk structures of g-C_3N_4, the preferential orientation of BiOBr is most likely influenced by the different surface charge of protonated g-C_3N_4, as it can influence the dispersion of Bi^{3+} on the surface to affect the nucleation and growth of BiOBr. A detailed explanation will be provided below.

The growth behavior not only changes the preferential orientation of BiOBr but also leads to varying microstructures of Bg-C_3N_4 and Bpg-C_3N_4-0.75. As demonstrated in Figure 2a, Bg-C_3N_4 is composed of two separated components. The nanoflowers assembled by many nanoflakes are BiOBr, whereas the micrometer lamellar materials are g-C_3N_4. The phase separation of these two components is further confirmed by the inhomogeneous elemental distribution. As shown in Figure 2b–f, Bi and Br elements are observed only in the region marked with a white circle, suggesting the agglomeration of BiOBr on the surface of g-C_3N_4. However, when BiOBr is supported on pg-C_3N_4-0.75, the situation changes. As

shown in Figure 3a, BiOBr nanoflakes with a diameter of ca. 10 nm are highly dispersed on the surface of pg-C_3N_4-0.75. The homogeneous distribution of Bi, Br, C, and N elements throughout Bg-C_3N_4-0.75 (Figure 3b–f) confirms the intimate contact between g-C_3N_4-0.75 and BiOBr. Semi-quantitative XPS analysis also suggests that Bpg-C_3N_4-0.75 exhibits higher surface Bi/N and Br/N ratios than Bg-C_3N_4. Taking the above results together, we conclude that the protonation of g-C_3N_4 significantly promotes the dispersion of supported BiOBr. Similar results were previously reported in an AgBr/g-C_3N_4 system. [25]

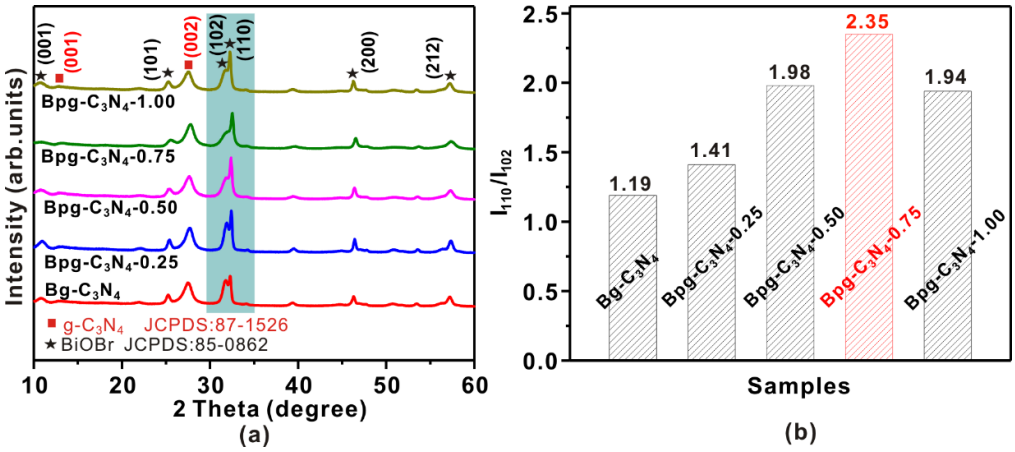

Figure 1. (**a**) XRD patterns and (**b**) the diffraction intensity ratio of (110)/(102) planes of Bg-C_3N_4 and Bpg-C_3N_4-X samples (X is the amount (in mL) of HCl added in the protonation treatment of g-C_3N_4; X = 0.25, 0.50, 0.75, 1.00).

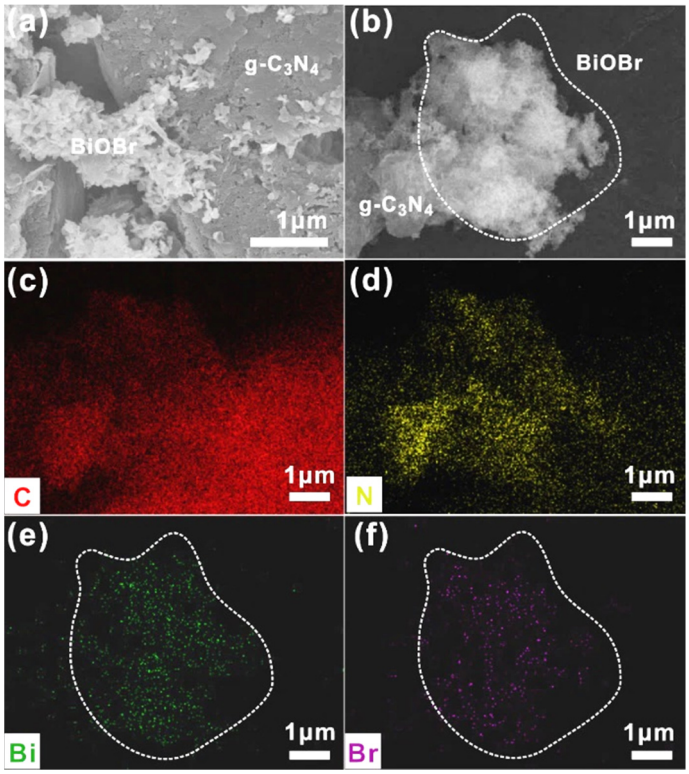

Figure 2. (**a**,**b**) SEM images and (**c**–**f**) element mapping of Bg-C_3N_4. The aggregated BiOBr nanoflowers are marked with white circle.

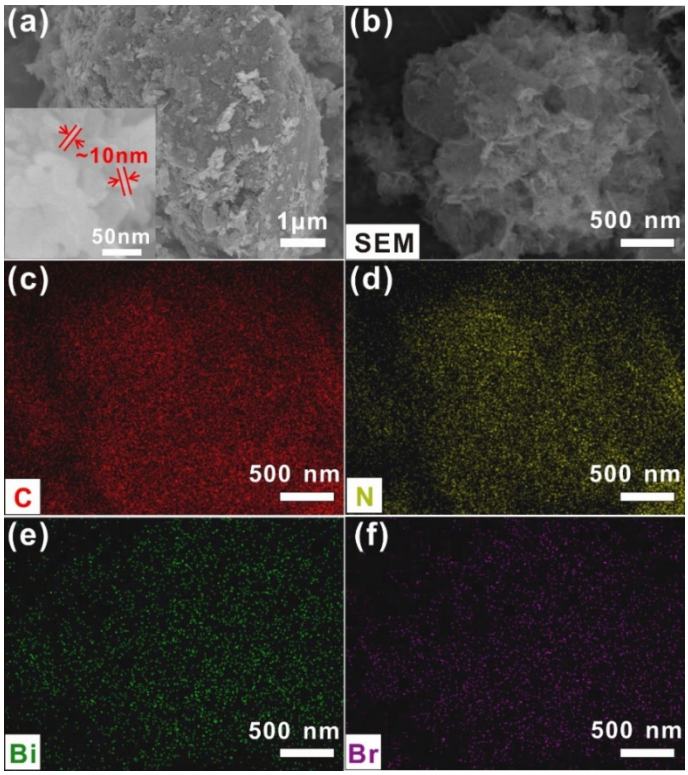

Figure 3. (**a**) SEM image (high-resolution image inset) and (**b**–**f**) element mapping of Bpg-C_3N_4-0.75.

In order to understand the support protonation effect on the growth behavior of BiOBr, we analyzed the zeta potential of pg-C_3N_4-X (Figure 4). In conventional studies [26], the protonation of g-C_3N_4 is usually conducted in strong acids with high concentration. The acid–base interaction between abundant –C–NH–/–C–NH_2 motifs in the g-C_3N_4 framework and H^+ usually changes the surface charge from negative to positive. [27] In this study, because the protonation of g-C_3N_4 was conducted in diluted HCl, only partial –C–NH–/–C–NH_2 motifs were protonated. As a result, g-C_3N_4-X samples are still negatively charged. With increased HCl concentration (i.e., the value of X), more –C–NH–/–C–NH_2 motifs are protonated, and the zeta potential increases accordingly. It is important to note that unprotonated –C–NH–/–C–NH_2 motifs can also serve as anchoring sites toward metal ions. In the deposition of BiOBr onto pg-C_3N_4, Bi^{3+}, ions are anchored by unprotonated –C–NH–/–C–NH_2 motifs before in situ reaction with Br^- to produce BiOBr. A high dispersion of Bi^{3+} on the surface of g-C_3N_4 enables a bounded nucleation and growth of BiOBr, which eventually leads to a high dispersion and preferential orientation of BiOBr perpendicular to the plane of the supports [7]. Notably, partial protonation of g-C_3N_4 is beneficial to the dispersion of Bi^{3+} because it can isolate the unprotonated –C–NH–/–C–NH_2 motifs. Excessively protonated –C–NH–/–C–NH_2 motifs, on the other hand, significantly decrease the anchoring sites of Bi^{3+}. The free Bi^{3+} may react with Br^- in solution to form aggregated BiOBr particles. To this end, median protonation is beneficial. In this study, the optimal HCl addition was determined to be 0.75 mL, as evidenced by the highest I_{110}/I_{102} ratio (Figure 1b) and the high dispersion of BiOBr revealed by SEM (Figure 3).

The high dispersion of BiOBr on pg-C_3N_4-0.75 produces abundant BiOBr/pg-C_3N_4-0.75 interfaces, which may promote the transfer and separation of photogenerated hole−electron pairs to improve the catalytic performance [5,7]. To verify this hypothesis, we investigated the photocurrent responses of Bg-C_3N_4 and Bpg-C_3N_4-0.75. As shown in Figure 5, both Bg-C_3N_4 and Bpg-C_3N_4-0.75 exhibit stable photocurrent response in the light on–off cycles. The photocurrent density of Bpg-C_3N_4-0.75 (0.11μA·cm^{-2}) is twice that of Bg-C_3N_4 (0.05 μA·cm^{-2}), confirming its superior separation and transfer of the photogenerated carriers. Notably, Bpg-C_3N_4-0.75 and Bg-C_3N_4 display similar Bi 4*f* XPS spectra (Figure 6a). The peaks located at

159.2 and 164.5 eV can be readily ascribed to Bi $4f_{5/2}$ and Bi $4f_{7/2}$ of BiOBr [12,28], suggesting that the protonated supports exert little influence on the valence states of the supported BiOBr. In addition, Bpg-C_3N_4-0.75 and Bg-C_3N_4 heterojunctions exhibit similar absorption responses in the visible region (Figure 6b), suggesting that the protonated supports have no impact on the light responses. Taking all above results together, the efficient separation of the photogenerated carriers of Bpg-C_3N_4-0.75 can be attributed to the abundant BiOBr/pg-C_3N_4-0.75 interfaces. The intimate contact between BiOBr and pg-C_3N_4-0.75 shortens the diffusion length of the photogenerated carriers, which enables a timely charge transfer between BiOBr and pg-C_3N_4-0.75 and inhibits the recombination of photogenerated carriers [29]. Similar results were reported in BiOI/ZnO systems in our previous publication [7].

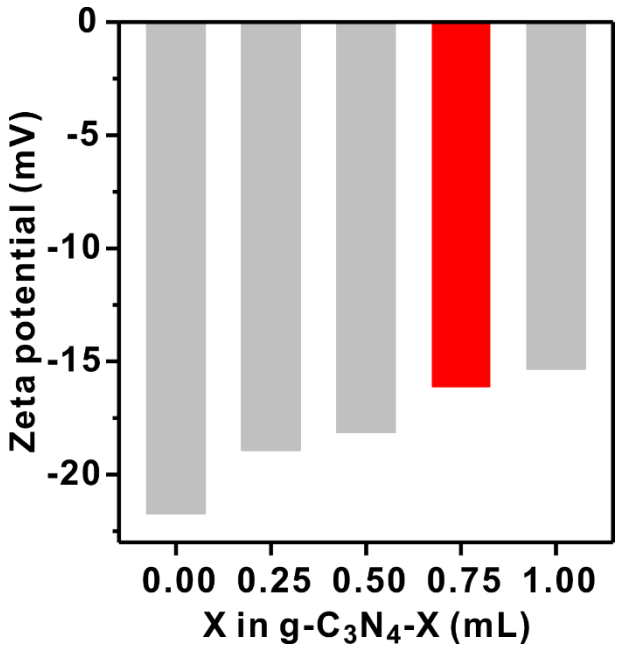

Figure 4. Zeta potential of g-C_3N_4-X samples.

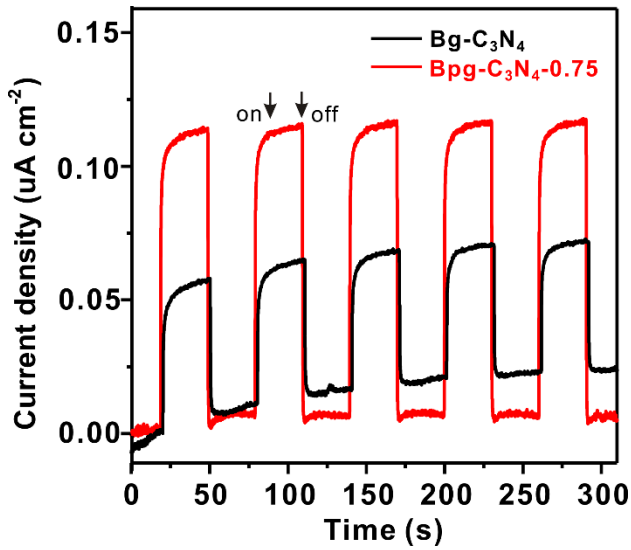

Figure 5. Photocurrent responses of Bg-C_3N_4 and Bpg-C_3N_4-0.75.

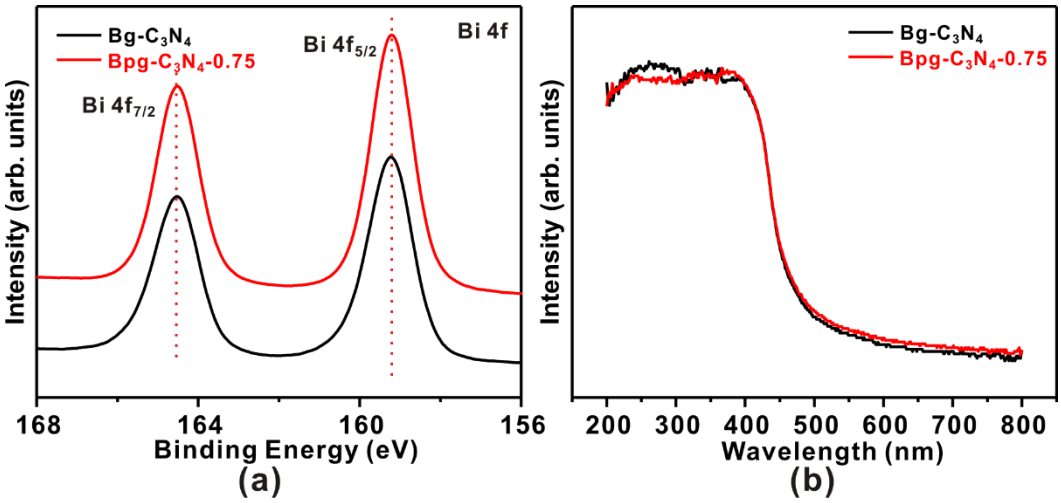

Figure 6. (**a**) Bi 4*f* spectra and (**b**) UV-Vis spectra of Bg-C_3N_4 and Bpg-C_3N_4-0.75.

The photocatalytic activities of the BiOBr/g-C_3N_4 heterojunctions were evaluated by the degradation of RhB under visible-light irradiation. As indicated in Figure 7a, both pure g-C_3N_4 and pg-C_3N_4-0.75 exhibit poor photocatalytic activity toward RhB degradation (less than 10% within 60 min). However, once BiOBr is loaded, the photocatalytic activity is considerably promoted. Bg-C_3N_4 degrades 50% of RhB within 60 min, which is significantly higher than that of g-C_3N_4. This improved activity originates from the formation of BiOBr/g-C_3N_4 heterojunctions, which facilitate the separation and transfer of photogenerated carriers. For the catalysts with BiOBr/g-C_3N_4 heterojunctions, the catalytic performance is determined by the different structure of g-C_3N_4. As shown in Figure 7a, the catalytic performance of BiOBr/g-C_3N_4 follows the trend of Bg-C_3N_4 < Bpg-C_3N_4-0.25 < Bpg-C_3N_4-0.50 < Bpg-C_3N_4-0.75 > Bpg-C_3N_4-1.00, which is consistent with the trend of the I_{110}/I_{102} ratio. In particular, the optimal Bpg-C_3N_4-0.75 catalyst degrades 96% of RhB within 60 min, which is significantly higher than that of Bg-C_3N_4. The photodegradation behavior of RhB over these samples can be fitted as the pseudo-first-order kinetics model (Figure 7b). Interestingly, the calculated rate constant (*k*) also follows the trend of Bg-C_3N_4 < Bpg-C_3N_4-0.25 < Bpg-C_3N_4-0.50 < Bpg-C_3N_4-0.75 > Bpg-C_3N_4-1.00 (Figure 7c), suggesting that the partial protonation of the support is beneficial to the photocatalytic performance. The highest *k* value observed on Bpg-C_3N_4-0.75 (0.045 min^{-1}) is ca. threefold higher than that on Bg-C_3N_4 (0.011 min^{-1}), demonstrating its superior photocatalytic performance. The degradation efficiency within 70 min of visible light irradiation remains higher than 95% in four consecutive runs (Figure 7d), indicating its excellent catalytic stability, which is consistent with the stable photocurrent response shown in Figure 5. Considering that Bpg-C_3N_4-0.75 and Bg-C_3N_4 have similar bulk structure of g-C_3N_4 (Figure 1a), surface area, valence state of BiOBr (Figure 6a), and visible-light absorption (Figure 6b), the superior photocatalytic activity of Bpg-C_3N_4-0.75 most likely originates from the high dispersion of BiOBr (Figure 3), which produces abundant BiOBr/g-C_3N_4 interfaces to promote the separation and transfer of photogenerated carriers (Figure 5). Regulating the amount of HCl added into the protonation of g-C_3N_4 modifies the surface charge of pg-C_3N_4, which eventually regulates the dispersion and the preferential orientation of supported BiOBr. The median protonation achieves the best BiOBr dispersion and the most BiOBr/g-C_3N_4 interfaces, which effectively separate and transfer the photogenerated carriers for efficient photocatalytic degradation of RhB.

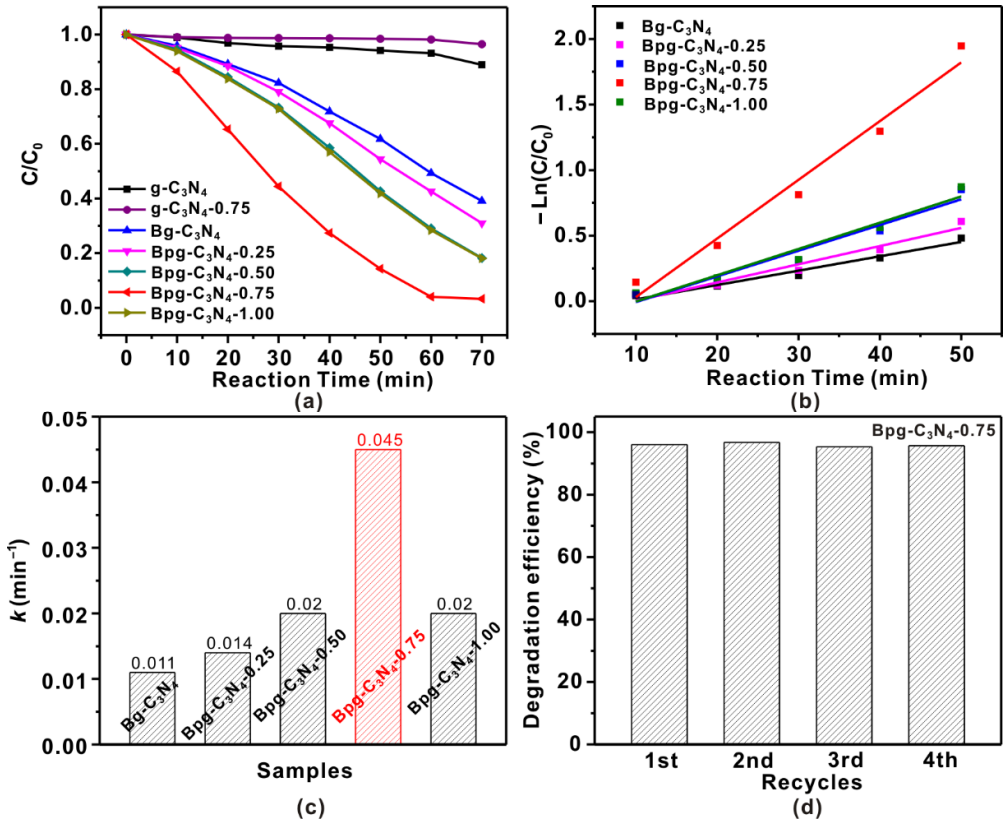

Figure 7. (**a**) Photodegradation of RhB (15 mg·L^{-1}) under visible-light irradiation ($\lambda \geq 420$ nm); (**b**) pseudo-first-order kinetic linear simulation lines; (**c**) the corresponding pseudo-first-order kinetic constants (*k*); (**d**) RhB degradation efficiency within 70 min of visible-light irradiation for four consecutive runs.

Radical-trapping experiments were further carried out to identify the active species involved in the photodegradation of RhB over Bpg-C_3N_4-0.75. As shown in Figure 8a, the addition of tert-butanol as a scavenger for $^{\bullet}OH$ radicals barely changes the degradation rate, excluding $^{\bullet}OH$ radicals as the main reactive oxygen species (ROS) involved in the reaction. In stark contrast, adding disodium ethylenediaminetetraacetate (Na_2-EDTA) and p-benzoquinone (BQ) as scavengers for h^+ and $O_2^{\bullet-}$ remarkably decreases the degradation efficiency, indicating that h^+ and $O_2^{\bullet-}$ are the key ROS involved in the photocatalytic degradation of RhB over Bpg-C_3N_4-0.75. According to the literature [30–32], the conduction band (CB) potential of BiOBr (0.22 eV vs NHE) is more positive than $E_0(O_2/O_2^{\bullet-} = -0.046$ eV vs NHE), so the photogenerated electrons of BiOBr barely react with O_2 to produce $O_2^{\bullet-}$. The reactive $O_2^{\bullet-}$ should therefore be produced by the reaction between O_2 and the photogenerated electrons of g-C_3N_4, of which the CB potential (−1.12 eV vs NHE) is more positive than $E_0(O_2/O_2^{\bullet-})$. On the other hand, the valence band (VB) potential of BiOBr is more positive than the VB potential of g-C_3N_4 and is thus more reactive toward the oxidation of RhB. Taken together, the BiOBr/g-C_3N_4 heterojunctions would prefer an S-scheme pathway (Figure 8b). [32] Specifically, when the junction is irradiated by visible light, electrons in the VB of both g-C_3N_4 and BiOBr are excited to their CB. Owing to the band bending, the built-in electric field, and Coulomb interactions, the photogenerated electrons in the CB of BiOBr will combine with the photogenerated holes in the VB of g-C_3N_4. The reserved electrons in the CB of g-C_3N_4 can react with O_2 to produce reactive $O_2^{\bullet-}$ for RhB degradation, whereas the reserved holes in the VB of BiOBr can oxidize RhB directly. Increasing BiOBr/g-C_3N_4 interfaces facilitates the combination of photogenerated electrons in the CB of BiOBr with the photogenerated holes in the VB of g-C_3N_4. As a result, more electrons in the CB of g-C_3N_4 and the holes in the VB of BiOBr can be used to produce ROS for RhB degradation.

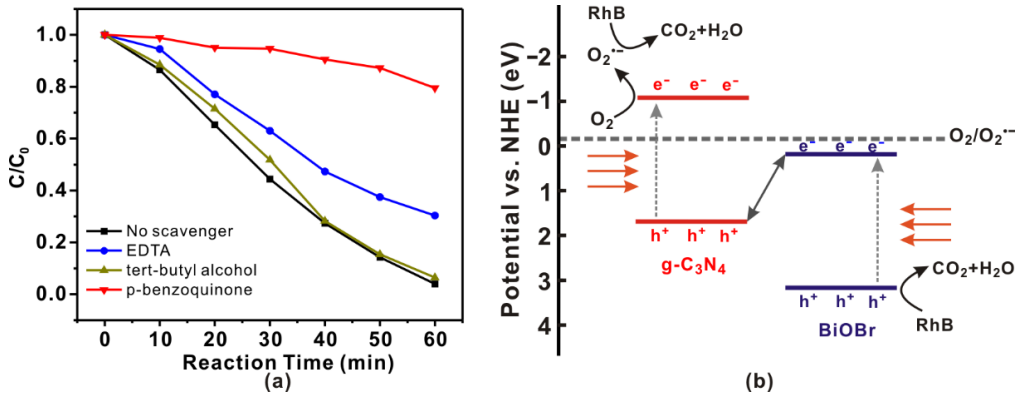

Figure 8. (**a**) The photodegradation of Bpg-C_3N_4-0.75 with different scavengers; (**b**) schematic illustration of the photodegradation of RhB over BiOBr/g-C_3N_4.

3. Materials and Methods

3.1. Preparation of Protonated g-C_3N_4 (pg-C_3N_4)

First, 3.0 g of melamine in a covered crucible was heated at 550 °C for 2 h to obtain g-C_3N_4. Subsequently, 0.3 g of the as-synthesized g-C_3N_4 was dispersed in 10 mL of water under stirring for 20 min at room temperature. Afterwards, certain amount of HCl (ca. 37 wt%, X mL, X = 0.25, 0.50, 0.75, 1.00) was added to the above suspension drop by drop. The mixture was stirred for 2 h for protonation. The solid products were collected and calcined in a covered crucible at 300 °C for 2 h to obtain the final products, which were designated as protonated g-C_3N_4-X (pg-C_3N_4-X, X = 0.25, 0.50, 0.75, 1.00).

3.2. Preparation of BiOBr-pg-C_3N_4-X (Bpg-C_3N_4-X) Heterojunctions

A volume of 10 mL of ethylene glycol dissolving 0.053 g of $Bi(NO_3)_3{\cdot}5H_2O$ was mixed with 8 mL of water containing 0.3 g of as-synthesized pg-C_3N_4-X. After vigorous stirring for 30 min, 2 mL of water containing 0.065 g of KBr was slowly added into the above mixture. After reaction for 1 h at room temperature, the solids were collected, washed, and dried. The product was labelled as Bpg-C_3N_4-X. BiOBr-g-C_3N_4 (Bg-C_3N_4) was synthesized using unprotonated g-C_3N_4 under the same conditions of Bpg-C_3N_4-0.75.

3.3. Characterizations

The crystal structure was studied on a Rigaku Ultimate IV diffractometer (Rigaku, Tokyo, Japan) using Cu Kα radiation. Scanning electron microscopy (SEM) and energy-dispersive X-ray spectrometric (EDX) microanalyses were performed on a Hitachi SU8100 (Hitachi, Tokyo, Japan). The specific surface area was measured by a nitrogen sorption analyzer (Micromeritics ASAP 2020, Norcross, GA, USA). The surface chemical states were verified by X-ray photoelectron spectroscopy (XPS, Thermo Scientific Escalab 250, Waltham, MA, USA). The Zeta potential of the samples was assessed using a Zetasizer Nano ZS (Malvern Instruments Ltd, Malvern, UK). UV-Vis diffuse reflectance spectra were measured using a Shimadzu UV-2450 (Shimadzu, Kyoto, Japan) spectrophotometer. The zero-biased photocurrent was measured using a CHI 660E electrochemical workstation (CHI instruments, Shanghai, China) with 0.1 M Na_2SO_4 solution as electrolyte. A 300 W Hg lamp with cutoff filters ($\lambda \geq 420$ nm) was utilized as a visible light source.

3.4. Photocatalytic Degradation of RhB

The visible-light photodegradation of RhB (15 mg·L^{-1}) at 25 °C was selected as the probe reaction to test the catalytic performances of as-synthesized heterojunctions. A high-pressure Hg lamp (300 W) with an optical filter ($\lambda \geq 420$ nm) was utilized as the light source. Briefly, 15 mg of catalyst and 50 mL of RhB solution were vigorously stirred in the dark for 60 min to achieve adsorption–desorption equilibrium. Afterwards, an appropriate amount of the suspension was extracted at given time intervals of light irradiation and centrifuged to remove

the solids. The concentration of RhB in the solution was detected by recording the absorbance at the characteristic band of 553 nm using a Shimadzu UV-2450 spectrophotometer.

3.5. Radical-Trapping Experiments

Radicals-trapping experiments were carried out in a similar manner as photocatalytic degradation. Disodium ethylenediaminetetraacetate (Na_2-EDTA), tert-butanol, and p-benzoquinone were used as scavengers to trap h^+, $^{\bullet}OH$, and $O_2^{\bullet-}$ radicals, respectively [5,7,24]. Prior to the photocatalytic test, 200 μL of scavengers (10 mM) was dripped into the reaction mixture once the mixture reached equilibrium. The suspension extracted at given time intervals under light irradiation was centrifuged and analyzed to obtain the concentration of pollutant.

4. Conclusions

In summary, a facile engineering of BiOBr/g-C_3N_4 heterojunction interface and its influence on the catalytic performances were reported herein. Protonating g-C_3N_4 in dilute HCl resulted in modification of surface charge without changing its bulk structure. When used as supports to load BiOBr, protonated g-C_3N_4 enabled high BiOBr dispersion and abundant BiOBr/g-C_3N_4 interfaces, which remarkably improved the separation and transfer of photogenerated carriers. The optimal catalyst, Bpg-C_3N_4-0.75, exhibited similar surface area, bulk g-C_3N_4 structure, and visible light absorption as Bg-C_3N_4, but its pseudo-first-order catalytic rate constant was ca. threefold higher than that of Bg-C_3N_4. These results verify interfacial engineering as an effective strategy to optimize the photocatalytic activity of heterojunctions.

Author Contributions: Conceptualization, J.L. and S.Z.; methodology, J.L.; validation, J.L., H.G. and Q.N.; investigation, J.L., H.G. and H.Y.; writing—original draft preparation, J.L.; writing—review and editing, S.Z.; visualization, J.L.; supervision, J.L. and S.Z.; project administration, J.L. and S.Z.; funding acquisition, J.L. and S.Z. All authors have read and agreed to the published version of the manuscript.

Funding: This work was financially supported by the National Natural Science Foundation of China (21703050, 21802122) and the Zhejiang Province Natural Science Foundation (LY22B030010).

Data Availability Statement: The data presented in this study are available upon request from the corresponding author.

Acknowledgments: The authors acknowledge Fang Chen for kind help in the scanning electron microscopy characterization.

Conflicts of Interest: The authors declare no conflict of interest.

References

1. Subhiksha, V.; Kokilavani, S.; Sudheer Khan, S. Recent advances in degradation of organic pollutant in aqueous solutions using bismuth based photocatalysts: A review. *Chemosphere* **2022**, *290*, 133228. [CrossRef] [PubMed]
2. Xu, Q.; Zhang, L.; Cheng, B.; Fan, J.; Yu, J. S-Scheme Heterojunction Photocatalyst. *Chem* **2020**, *6*, 1543–1559. [CrossRef]
3. Liu, H.; Du, C.; Li, M.; Zhang, S.; Bai, H.; Yang, L.; Zhang, S. One-pot hydrothermal synthesis of SnO_2/BiOBr heterojunction photocatalysts for the efficient degradation of organic pollutants under visible light. *ACS Appl. Mater. Interf.* **2018**, *10*, 28686–28694. [CrossRef]
4. Shi, Z.; Zhang, Y.; Shen, X.; Duoerkun, G.; Zhu, B.; Zhang, L.; Li, M.; Chen, Z. Fabrication of g-C_3N_4/BiOBr heterojunctions on carbon fibers as weaveable photocatalyst for degrading tetracycline hydrochloride under visible light. *Chem. Eng. J.* **2020**, *386*, 124010. [CrossRef]
5. Liu, J.; Zhou, J.; Yin, H.; Zhao, H. One-pot synthesis of 3D flower-like Bi_2S_3/BiOCl heterostructures at room temperature with enhanced visible-light photocatalytic activity. *Mater. Lett.* **2019**, *255*, 126568. [CrossRef]
6. Yang, L.; Liang, L.; Wang, L.; Zhu, J.; Gao, S.; Xia, X. Accelerated photocatalytic oxidation of carbamazepine by a novel 3D hierarchical protonated g-C_3N_4/BiOBr heterojunction: Performance and mechanism. *Appl. Surf. Sci.* **2019**, *473*, 527–539. [CrossRef]
7. Liu, J.; Zou, S.; Lou, B.; Chen, C.; Xiao, L.; Fan, J. Interfacial electronic interaction induced engineering of ZnO-BiOI heterostructures for efficient visible-light photocatalysis. *Inorg. Chem.* **2019**, *58*, 8525–8532. [CrossRef]
8. Tang, Q.-Y.; Yang, M.-J.; Yang, S.-Y.; Xu, Y.-H. Enhanced photocatalytic degradation of glyphosate over 2D CoS/BiOBr heterojunctions under visible light irradiation. *J. Hazard. Mater.* **2021**, *407*, 124798. [CrossRef]

9. Pham, T.-T.; Shin, E.W. Influence of g-C_3N_4 Precursors in g-C_3N_4/$NiTiO_3$ Composites on Photocatalytic Behavior and the Interconnection between g-C_3N_4 and $NiTiO_3$. *Langmuir* **2018**, *34*, 13144–13154. [CrossRef]
10. Su, T.; Hood, Z.D.; Naguib, M.; Bai, L.; Luo, S.; Rouleau, C.M.; Ivanov, I.N.; Ji, H.; Qin, Z.; Wu, Z. 2D/2D heterojunction of Ti_3C_2/g-C_3N_4 nanosheets for enhanced photocatalytic hydrogen evolution. *Nanoscale* **2019**, *11*, 8138–8149. [CrossRef]
11. Peng, R.; Kang, Y.; Deng, X.; Zhang, X.; Xie, F.; Wang, H.; Liu, W. Topotactic transformed face-to-face heterojunction of BiOCl/Bi_2WO_6 for improved tetracycline photodegradation. *J. Environ. Chem. Eng.* **2021**, *9*, 106750. [CrossRef]
12. Yang, Z.; Li, J.; Cheng, F.; Chen, Z.; Dong, X. BiOBr/protonated graphitic C_3N_4 heterojunctions: Intimate interfaces by electrostatic interaction and enhanced photocatalytic activity. *J. Alloy. Compd.* **2015**, *634*, 215–222. [CrossRef]
13. Dong, F.; Zhao, Z.; Xiong, T.; Ni, Z.; Zhang, W.; Sun, Y.; Ho, W.-K. In situ construction of g-C_3N_4/g-C_3N_4 metal-free heterojunction for enhanced visible-light photocatalysis. *ACS Appl. Mater. Interf.* **2013**, *5*, 11392–11401. [CrossRef] [PubMed]
14. Wang, X.; Maeda, K.; Thomas, A.; Takanabe, K.; Xin, G.; Carlsson, J.M.; Domen, K.; Antonietti, M. A metal-free polymeric photocatalyst for hydrogen production from water under visible light. *Nat. Mater.* **2009**, *8*, 76–80. [CrossRef] [PubMed]
15. Fu, J.; Yu, J.; Jiang, C.; Cheng, B. g-C_3N_4-Based Heterostructured Photocatalysts. *Adv. Energ. Mater.* **2018**, *8*, 1701503. [CrossRef]
16. Ong, W.-J.; Tan, L.-L.; Ng, Y.H.; Yong, S.-T.; Chai, S.-P. Graphitic Carbon Nitride (g-C_3N_4)-Based Photocatalysts for Artificial Photosynthesis and Environmental Remediation: Are We a Step Closer To Achieving Sustainability? *Chem. Rev.* **2016**, *116*, 7159–7329. [CrossRef]
17. Li, Y.; Gu, M.; Zhang, X.; Fan, J.; Lv, K.; Carabineiro, S.A.C.; Dong, F. 2D g-C_3N_4 for advancement of photo-generated carrier dynamics: Status and challenges. *Mater. Today* **2020**, *41*, 270–303. [CrossRef]
18. Ye, C.; Li, J.-X.; Li, Z.-J.; Li, X.-B.; Fan, X.-B.; Zhang, L.-P.; Chen, B.; Tung, C.-H.; Wu, L.-Z. Enhanced driving force and charge separation efficiency of protonated g-C_3N_4 for photocatalytic O_2 evolution. *ACS Catal.* **2015**, *5*, 6973–6979. [CrossRef]
19. Dasary, S.S.; Singh, A.K.; Senapati, D.; Yu, H.; Ray, P.C. Gold nanoparticle based label-free SERS probe for ultrasensitive and selective detection of trinitrotoluene. *J. Am. Chem. Soc.* **2009**, *131*, 13806–13812. [CrossRef] [PubMed]
20. Cheng, F.; Wang, H.; Dong, X. The amphoteric properties of g-C_3N_4 nanosheets and fabrication of their relevant heterostructure photocatalysts by an electrostatic re-assembly route. *Chem. Commun.* **2015**, *51*, 7176–7179. [CrossRef] [PubMed]
21. Ge, L. Synthesis and photocatalytic performance of novel metal-free g-C_3N_4 photocatalysts. *Mater. Lett.* **2011**, *65*, 2652–2654. [CrossRef]
22. Li, R.; Ren, H.; Ma, W.; Hong, S.; Wu, L.; Huang, Y. Synthesis of BiOBr microspheres with ethanol as self-template and solvent with controllable morphology and photocatalytic activity. *Catal. Commun.* **2018**, *106*, 1–5. [CrossRef]
23. Sun, X.; Zhao, H.; Li, H.; Cai, T.; Li, M.; Wang, Y. BiOI With High Intensity Ratio of (110)/(102) Facets and Iodine Vacancies: Facile Synthesis, Strong Adsorption and Visible-Light Photocatalytic Performance. *ChemistrySelect* **2021**, *6*, 13319–13326. [CrossRef]
24. Liu, J.; Zhang, S.; Zhao, H. Fabricating visible-light photoactive 3D flower-like BiOCl nanostructures via a one-step solution chemistry method at room temperature. *Appl. Surf. Sci.* **2019**, *479*, 247–252. [CrossRef]
25. Feng, Y.; Shen, J.; Cai, Q.; Yang, H.; Shen, Q. The preparation and properties of a g-C_3N_4/AgBr nanocomposite photocatalyst based on protonation pretreatment. *N. J. Chem.* **2015**, *39*, 1132–1138. [CrossRef]
26. Ong, W.-J.; Tan, L.-L.; Chai, S.-P.; Yong, S.-T.; Mohamed, A.R. Surface charge modification via protonation of graphitic carbon nitride (g-C_3N_4) for electrostatic self-assembly construction of 2D/2D reduced graphene oxide (rGO)/g-C_3N_4 nanostructures toward enhanced photocatalytic reduction of carbon dioxide to methane. *Nano Energy* **2015**, *13*, 757–770. [CrossRef]
27. Zhang, Y.; Thomas, A.; Antonietti, M.; Wang, X. Activation of Carbon Nitride Solids by Protonation: Morphology Changes, Enhanced Ionic Conductivity, and Photoconduction Experiments. *J. Am. Chem. Soc.* **2009**, *131*, 50–51. [CrossRef] [PubMed]
28. Bao, Y.; Chen, K. Novel Z-scheme BiOBr/reduced graphene oxide/protonated g-C_3N_4 photocatalyst: Synthesis, characterization, visible light photocatalytic activity and mechanism. *Appl. Surf. Sci.* **2018**, *437*, 51–61. [CrossRef]
29. Yang, H.; Cao, R.; Sun, P.; Yin, J.; Zhang, S.; Xu, X. Constructing electrostatic self-assembled 2D/2D ultra-thin $ZnIn_2S_4$/protonated g-C_3N_4 heterojunctions for excellent photocatalytic performance under visible light. *Appl. Catal. B* **2019**, *256*, 117862. [CrossRef]
30. Liang, Y.; Zeng, Z.; Yang, J.; Yang, G.; Han, Y. Designing heterointerface in BiOBr/g-C_3N_4 photocatalyst to enhance visible-light-driven photocatalytic performance in water purification. *Colloids Surf. A* **2021**, *624*, 126796. [CrossRef]
31. Ye, L.; Liu, J.; Jiang, Z.; Peng, T.; Zan, L. Facets coupling of BiOBr-g-C_3N_4 composite photocatalyst for enhanced visible-light-driven photocatalytic activity. *Appl. Catal. B Environ.* **2013**, *142–143*, 1–7. [CrossRef]
32. Zhang, B.; Hu, X.; Liu, E.; Fan, J. Novel S-scheme 2D/2D BiOBr/g-C_3N_4 heterojunctions with enhanced photocatalytic activity. *Chin. J. Catal.* **2021**, *42*, 1519–1529. [CrossRef]